nanomaterials

MDPI

Article

Unveiling $BaTiO_3$-$SrTiO_3$ as Anodes for Highly Efficient and Stable Lithium-Ion Batteries

Nischal Oli [1,*], Nawraj Sapkota [2], Brad R. Weiner [3], Gerardo Morell [1] and Ram S. Katiyar [1,*]

[1] Department of Physics, University of Puerto Rico-Rio Piedras Campus, San Juan, PR 00925, USA
[2] Department of Physics and Astronomy, Clemson University, Clemson, SC 29634, USA
[3] Department of Chemistry, University of Puerto Rico-Rio Piedras Campus, San Juan, PR 00925, USA
* Correspondence: nischal.oli@upr.edu (N.O.); ram.katiyar@upr.edu (R.S.K.)

Abstract: Amidst the swift expansion of the electric vehicle industry, the imperative for alternative battery technologies that balance economic feasibility with sustainability has reached unprecedented importance. Herein, we utilized Perovskite-based oxide compounds barium titanate ($BaTiO_3$) and strontium titanate ($SrTiO_3$) nanoparticles as anode materials for lithium-ion batteries from straightforward and standard carbonate-based electrolyte with 10% fluoroethylene carbonate (FEC) additive [1M $LiPF_6$ (1:1 EC: DEC) + 10% FEC]. $SrTiO_3$ and $BaTiO_3$ electrodes can deliver a high specific capacity of 80 mA h g^{-1} at a safe and low average working potential of ≈0.6 V vs. Li/Li^+ with excellent high-rate performance with specific capacity of ~90 mA h g^{-1} at low current density of 20 mA g^{-1} and specific capacity of ~80 mA h g^{-1} for over 500 cycles at high current density of 100 mA g^{-1}. Our findings pave the way for the direct utilization of perovskite-type materials as anode materials in Li-ion batteries due to their promising potential for Li^+ ion storage. This investigation addresses the escalating market demands in a sustainable manner and opens avenues for the investigation of diverse perovskite oxides as advanced anodes for next-generation metal-ion batteries.

Keywords: $BaTiO_3$; $SrTiO_3$; perovskite-type materials; high-rate performance; lithium-ion batteries

check for updates

Citation: Oli, N.; Sapkota, N.; Weiner, B.R.; Morell, G.; S. Katiyar, R. Unveiling $BaTiO_3$-$SrTiO_3$ as Anodes for Highly Efficient and Stable Lithium-Ion Batteries. *Nanomaterials* **2024**, *14*, 1723. https://doi.org/10.3390/nano14211723

Academic Editor: Jung Woo Lee

Received: 17 September 2024
Revised: 26 October 2024
Accepted: 27 October 2024
Published: 29 October 2024

Copyright: © 2024 by the authors. Licensee MDPI, Basel, Switzerland. This article is an open access article distributed under the terms and conditions of the Creative Commons Attribution (CC BY) license (https://creativecommons.org/licenses/by/4.0/).

1. Introduction

A gift to modern humanity, lithium-ion batteries (LIBs) embodied by high energy and power density, enhanced safety features, and prolonged life cycles are presently propelling advancements in the domain of portable electronics, automobiles, electric vehicles (EVs) and hybrid electric vehicles (HEVs) [1–4]. Exploring novel stable materials for negative electrodes is essential for improving the performance of LIBs [5–8]. This is accomplished through the utilization of lithium-alloy materials such as tin, germanium, silicon, phosphorus, and lithium metal [9–13]. Regrettably, lithium-alloying reactions exhibit substantially large volume expansion of ~300%, resulting in significant capacity deterioration in a few cycles. The enhancement of cycle stability in rechargeable lithium-ion batteries is pursued through the design and implementation of advanced composite materials [14]. Pointedly, composite configurations such as silicon–graphite/carbon hybrids [15], red phosphorus–carbon [16], black phosphorus–graphite [17], and tin–graphene [18] are researched as effective avenues for improvement. In contrast to lithium-alloy anode materials, lithium-intercalation anode materials, mainly commercial graphite, exhibit minimal volume change during lithiation–delithiation [19]. However, graphite encounters challenges arising from poor intercalation kinetics and lithium plating phenomena, particularly fast charging at high current and low temperature [20]. These issues emanate from graphite's low lithiation potential (≈0.01 V vs. Li/Li^+), which turn out to be safety concerns related to dendritic lithium growth [21]. Thus, the average working voltage needs to be high enough to prevent Li plating but still low enough to accomplish a high full cell output potential. Titanium-based anode material $Li_4Ti_5O_{12}$ [22,23] and niobium-based anode

materials ($W_5Nb_{16}O_{55}$, $Cu_2Nb_{34}O_{87}$, Nb_2O_5, etc.) exhibit high-rate performance and extended cycle stability [24,25]. However, these materials face challenges such as low output voltage and poor electronic conductivity. The synthesis of intercalation-type anode materials with simultaneously high intrinsic electronic and ionic conductivity while preserving essential properties poses a significant hurdle in advancing the utilization of anodes in lithium-ion batteries.

In light of these challenges, it is imperative to explore advanced novel materials. One promising class of compounds is perovskites with the ABO_3 structure, characterized by large A-site cations positioned at the central lattice, which play a crucial role in stabilizing the overall framework. Its unique corner-sharing BO_6 structure creates three-dimensional (3D) networks facilitating rapid Li^+ transport and ensuring high ionic conductivity [26]. The perovskite family of anode materials presents a promising avenue for enhancing lithium-ion battery (LIB) performance, with specific emphasis on compounds such as $La_{0.5}Li_{0.5}TiO_3$ [27], $NdMnxFe_{1-x}O_3$ [28], $SrVO_3$ [29], $BiFeO_3$ [5], $CaMnO_3$ [30], $RMnO_3$ (where R represents La, Nd, or Eu) [31], and $LiNbO_3$ where the amorphous LiNbO3 films demonstrate impressive gravimetric capacity during rapid cycling. Notably, these films were cycled without the need for any conductive additives [32], indicating that they possess excellent intrinsic electronic conductivity and high Li^+ ion diffusivity, attributed to their amorphous structure [32]. These materials exhibit significant electrochemical properties conducive to lithium storage and cycling stability. Noteworthy candidates also include $Na_{0.5}Bi_{0.5}TiO_3$ [33] and hollow spherical $LaFeO_3$ [34], alongside $CeMnO_3$ nanofibers [35] and double perovskite configurations like La_2MnNiO_6 [36]. Hybrid perovskite-like iodobismuthates as low-cost and stable anode materials [37], highly stable metal halide perovskite microcube anodes for lithium-air batteries [38], perovskite oxides with Pb at B-site [39], photorechargeable lead-free perovskite lithium-ion batteries using hexagonal $Cs_3Bi_2I_9$ nanosheets [40], a microstructure engineered perovskite super anode with Li-storage life of exceeding 10,000 cycles [41]. Despite their potential, the exploration of perovskite materials as battery anode has been notably limited. $SrTiO_3$ as an anode only studied by Derek C. Johnson and Amy L. Prieto in LIBs revealed a specific capacity below 100 mA h g^{-1} at a working potential of ~1 V vs. Li/Li^+ and with lithiation potentials 0.105 V and 0.070 V vs. Li/Li^+ and 0.095 Vand 0.142 V vs. Li/Li^+ during delithiation [42]. The cyclability was reported to be less than 35 cycles, and capacity faded rapidly. But, $BaTiO_3$ has not been researched yet as an anode for LIBs. Thus, exploring $SrTiO_3$ and $BaTiO_3$ offers opportunities to enhance the capacity and rate capability of LIBs anodes. It reveals the arena of novel compounds as substitutes for the existing graphite anode. Here, we report that the $SrTiO_3$ and $BaTiO_3$ electrodes exhibit a high specific capacity of 90 mA h g^{-1} at a low current density of 20 mA g^{-1}, a safe and low average working potential of ~0.6 V vs. Li/Li^+, which is higher than graphite anode (Supplementary Information Figure S5) while also demonstrating excellent high-rate performance, maintaining a capacity of ~80 mA h g^{-1} over 500 cycles at high current density of 100 mA g^{-1} by both compound. These findings highlight the potential of perovskite-type materials as promising candidates for anode applications in Li-ion batteries, given their capacity for efficient Li^+ ion storage.

2. Experimental Section

2.1. Synthesis of Electrode Materials

The electrode materials were synthesized via a commercially feasible ball mill approach. Initially, commercially available $BaTiO_3$ (Sigma Aldrich, nanopowder 99.99%, St. Louis, MO, USA) and $SrTiO_3$ (Sigma Aldrich, nanopowder 99%, St. Louis, MO, USA) were utilized. These materials were then mixed in a ratio of 7:2 with carbon super P and subjected to grinding for an hour.

2.2. Materials Characterizations

Scanning electron microscopy—energy dispersive spectroscopy (SEM-EDS) analyses were performed utilizing JEOL, model JSM 6480 LV, Tokyo, Japan. X-ray diffraction (XRD)

measurements were conducted employing a Rigaku SmartLab system, using Cu Kα radiation with a wavelength (λ) of 1.5408 Å, scanning within the range of 20 to 80 degrees at a rate of 2 degrees per minute. Raman spectra were attained using a T64000 Raman spectrometer from Instrument S.A., Jobin Yvon -Horiba (Longjumeau, France) Triple monochromator in subtractive mode equipped with a CCD detector. An Olympus microscope focused with an 80X objective in backscattering mode. The laser is Coherent Argon Innova 70C using 514.53 nm and 5 mW on the sample.. X-ray photoelectron spectroscopy (XPS) has also been performed to analyze detailed insights into the elemental composition and the chemical and electronic states of atoms. XPS data were collected using a PHI VersaProbe III with a monochromatic Al Kα X-ray source (hν = 1486.6 eV) and an Al anode powered at 25 W and 15 kV.

2.3. Electrochemical Analysis

In order to analyze the electrochemical performance, the slurry was prepared by mixing active materials ($BaTiO_3$ and $SrTiO_3$) with Super P carbon black as a conductive agent and Poly (vinylidene fluoride) (PVDF) binder in N-Methyl-2-pyrrolidone (NMP) in a weight ratio of 70:20:10, respectively. The prepared slurry was coated on 9 µm copper foil using a doctor-blade (MTI Corporation, Richmond, CA, USA). The coated electrodes were dried in a vacuum oven at 110 °C for 12 h. The battery performance of the electrodes was assessed by punching out 10 mm coupons and using them as the working electrode for CR2032 coin cells. Polypropylene Celgard was used as the separator, and lithium (Li) metal served as the counter/reference electrode. The electrolyte for the lithium-ion cell was 1 M $LiPF_6$ in ethylene carbonate (EC)/dimethyl carbonate (DMC) [1:1 (v/v)] containing 10 wt.% of fluoroethylene carbonates (FEC) as an additive [1 M $LiPF_6$/EC-DMC + 10% FEC]. The active materials ($BaTiO_3$ and $SrTiO_3$) had a loading of around 1.91–2.23 mg cm^{-2} with a thickness of 15–20 µm. Charge/discharge performance was evaluated with a Landt battery tester in the voltage window of 0.001–1.5 V, 0.001–2 V, and 0.001–2.5 V. The coin cells (CR2032) were assembled in an Ar-filled glove box (MBRAUN, Glovebox Workstations, Stratham, NH, USA) with H_2O and O_2 contents < 0.1 ppm. Fabricated coin cells were tested at various current densities using a Landt instruments battery tester (Hudson, NY, USA). Cyclic voltammetry was tested with an Arbin instrument at a scan rate of 0.1–1.2 mV s^{-1} range at 0.001–1.5 V.

3. Result and Discussions

The STO sample demonstrates itself as a fine whitish powder (Figure 1a, inset). The X-ray diffraction (XRD) pattern, depicted in Figure 1a, reveals that all observed diffraction peaks correspond to a cubic perovskite structure with space group Pm3m (#211) and a lattice constant of a = 3.90 Å, aligning with the reference value (JCPDS: 35-0734) [43]. The pronounced peaks are indicative of a high degree of crystallinity, and it has no phase impurities. The cubic crystal structure of STO is illustrated in Figure 1b, where Sr^{2+} ions are coordinated to twelve oxygen atoms, and Ti^{4+} ions are octahedrally coordinated to six oxygen atoms [44]. Figure 1c presents the Raman spectrum of the STO sample, exhibiting characteristic Raman shifts that align well with the typical Raman peaks associated with STO [45]. Moreover, the substantial mass of Sr^{2+} and Ti^{4+} ions results in a high crystal density of 5.1 g cm^{-3} [46], significantly surpassing that of graphite, thereby enhancing volumetric energy density.

Similarly, the BTO sample is a fine white powder (Figure 1d, inset). The XRD pattern indicated in Figure 1d can be readily indexed to the tetragonal BTO phase (JCPDS no. 01-075-0583) with lattice parameters a = b = 3.9950 Å and c = 4.0340 Å and crystallizes in the tetragonal P4mm (# 99) space group [47]. The well-defined peaks confirm a high degree of crystallinity and high purity in the BTO sample. BTO is a (Cubic) perovskite structure [48] shown in Figure 1e. Figure 1f illustrates the Raman spectrum of the BTO sample, displaying characteristic Raman shifts that correspond closely to the standard Raman peaks of BTO [49]. Moreover, the presence of Ba^{2+} and Ti^{4+} ions contributes to a

high crystal density of 6.02 g cm^{-3} [50], which is substantially higher than that of graphite, thus enhancing volumetric energy density.

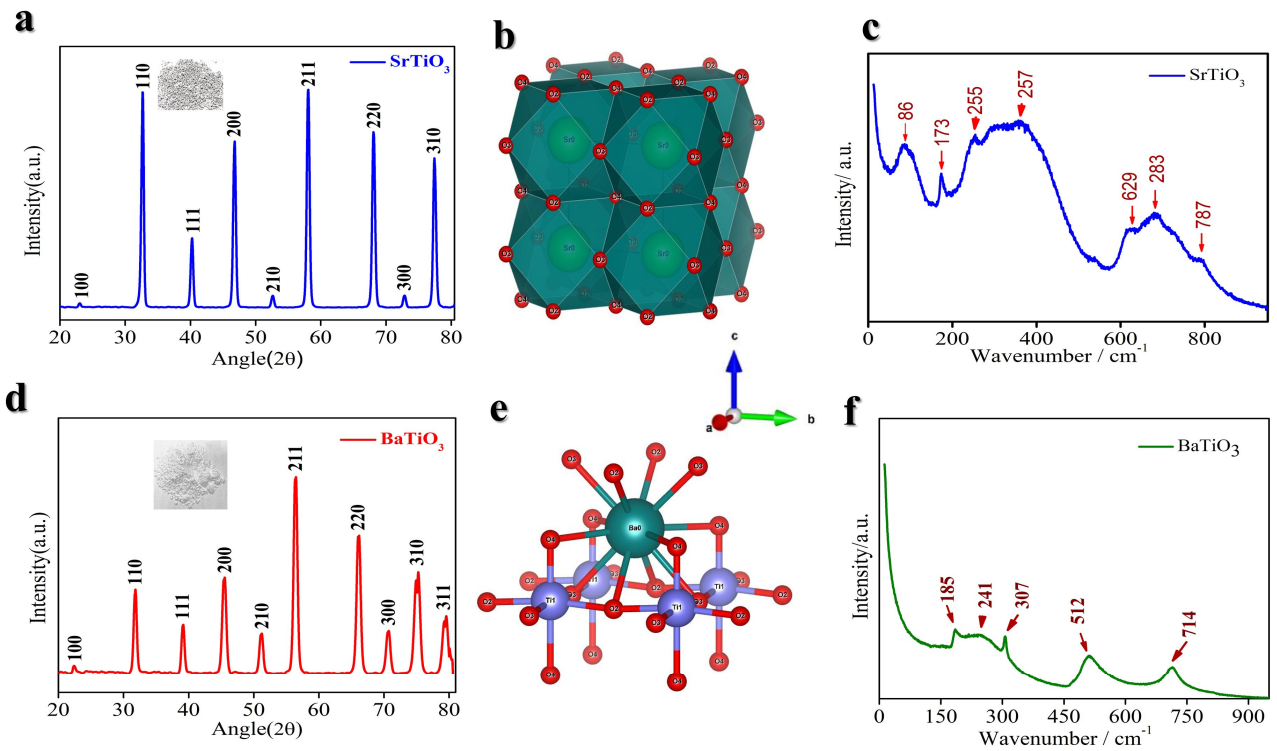


Figure 1. (**a**) XRD pattern $SrTiO_3$ (STO). (**b**) Crystal structure of STO. (**c**) Raman shifts of STO. (**d**) XRD pattern of $BaTiO_3$ (BTO). (**e**) Crystal structure of BTO. (**f**) Raman shifts of BTO.

Figure 2a,b illustrate the morphology of the BTO nanocrystallites. The SEM images clearly depict randomly distributed grains of smaller sizes, along with uniform spherical particles. These images reveal that the average crystalline size ranges between 20 and 100 nm.

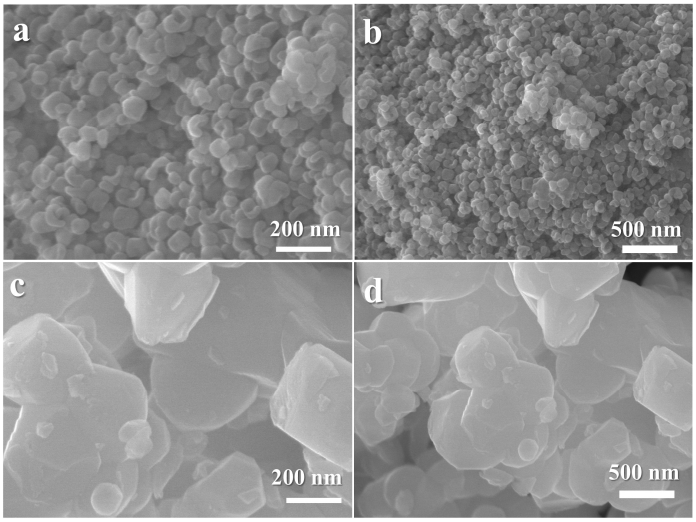


Figure 2. SEM images of BTO and STO. (**a**) BTO at 200 nm. (**b**) BTO at 500 nm. (**c**) STO at 200 nm. (**d**) STO at 500 nm.

Moreover, for STO, Figure 2c,d present SEM images, revealing particles with irregular polyhedral shapes (100–200 nm) and numerous nanosteps, consistent. The sequential

layering of the particles creates a porous structure that could facilitate efficient pathways for lithium-ion migration.

Figure 3a–d display the element mapping of BTO nanopowder, where different colors represent the distribution of Ba, Ti, and O. The EDX pattern, detailed in the (Supplementary Information Figure S1), confirms the presence of each constituent element. Both analyses indicate that BTO is uniformly distributed.

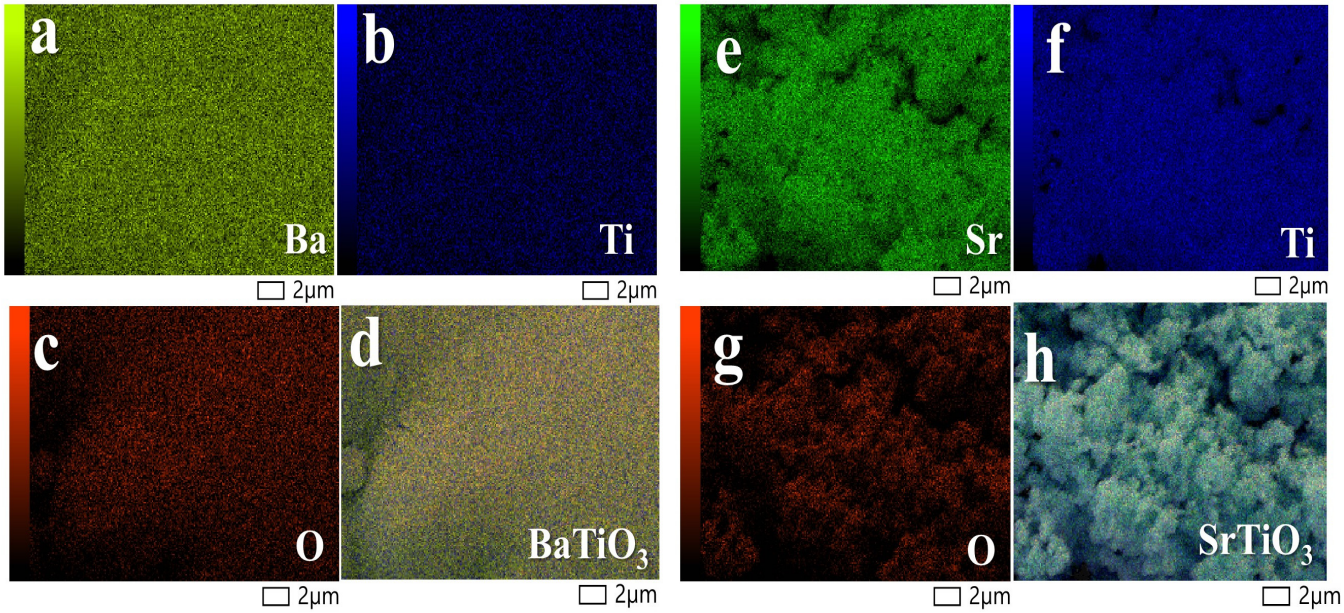


Figure 3. SEM mapping images of BTO and STO at 2 μm. (**a**–**d**) Ba, Ti, O, and $BaTiO_3$, respectively. (**e**–**h**) Sr, Ti, O, and $SrTiO_3$, respectively.

Likewise, Figure 3e–h show the elemental mapping of STO nanopowder, with distinct colors illustrating the spatial distribution of Sr, Ti, and O. The EDX pattern, provided in the (Supplementary Information Figure S2), verifies the presence of each constituent element. Both sets of data corroborate the uniform distribution of STO.

We investigated the lithium storage capabilities of BTO (1C = 114 mA g^{-1}) (in detail calculation of theoretical capacity are in Supplementary Information Page S-6) when used as an anode material for lithium-ion batteries (LIBs). The electrochemical performance of BTO was tested in three different voltage ranges: 0.001–1.5 V, 0.001–2.0 V, and 0.001–2.5 V, at room temperature. As depicted in Figure 4a, the GCD curve for the 0.001–1.5 V range shows a discharge capacity of ~200 mA h g^{-1}, while the charge capacity is 70 mA h g^{-1}, remaining stable over 500 cycles with ~99.99% coulombic efficiency, as shown in Figure 4b. In Figure 4c, the GCD curve for the 0.001–2.0 V range indicates a specific capacity of about 80 mA h g^{-1}, which is maintained for over 500 cycles, as demonstrated in Figure 4d. Additionally, we tested the charge–discharge performance at 0.001–2.5 V, but there is no significant difference we observed, as shown in (Supplementary Information Figure S3b). However, cycling performance is poor, as demonstrated in (Supplementary Information Figure S4b).

Similarly, we explored the lithium storage capabilities of STO (1C = 146 mA g^{-1}) (in detail in Supplementary Information Page S-6). The electrochemical performance of STO was evaluated across three distinct voltage ranges: 0.001–1.5 V, 0.001–2.0 V, and 0.001–2.5 V, all measured at room temperature. As illustrated in Figure 5a, the GCD curve for the 0.001–1.5 V range exhibits a discharge capacity of approximately 200 mA h g^{-1}, with a corresponding charge capacity of 70 mA h g^{-1}, demonstrating stability over 500 cycles with ~99.99% coulombic efficiency, as shown in Figure 5b. In Figure 5c, the GCD curve for the 0.001–2.0 V range indicates a specific capacity of around 80 mA h g^{-1}, which is sustained over 500 cycles, as evidenced in Figure 5d. Furthermore, the charge–discharge

response at 0.001–2.5 V was examined, revealing no significant differences, as depicted in the GCD curve ((Supplementary Information Figure S3a)) but poor cycling performance, as shown in (Supplementary Information Figure S4a).

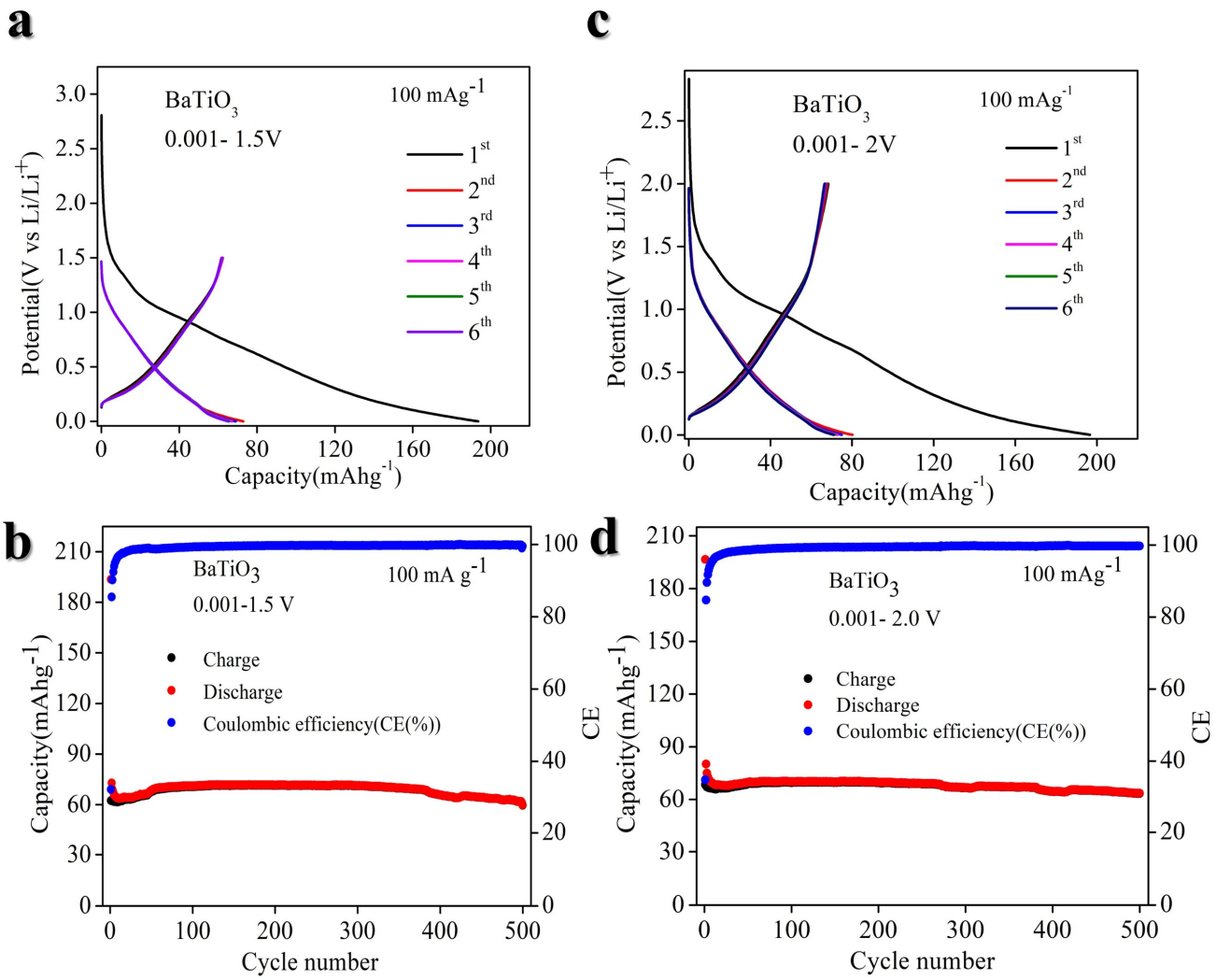


Figure 4. Electrochemical performance of BTO at different voltage ranges in LIBs. (**a**) Galvanostatic charge–discharge (GCD) at 0.001–1.5 V. (**b**) Cyclic performance at 0.001–1.5 V. (**c**) Galvanostatic charge–discharge (GCD) at 0.001–2.0 V. (**d**) Cyclic performance at 0.001–2.0 V.

To understand rate capability, Figure 6a,b show the rate performance of STO and BTO at a current density ranging from 20 mA g^{-1} to 150 mA g^{-1}. The data unequivocally demonstrate that both materials exhibit superior rate performance.

In regard to STO rate performance, as shown in Figure 6a,b, the discharge capacity is ~90 mA h g^{-1} at a low current density of 20 mA g^{-1}, and the discharge capacity is 63 mA h g^{-1}, 52 mA h g^{-1}, and 50 mA h g^{-1} at the current density of 50 mA g^{-1}, 100 mA g^{-1}, and 150 mA g^{-1}, respectively. When the current returns to 20 mA g^{-1}, the discharge capacity can maintain a value of ~86 mA h g^{-1}.

Similarly, for BTO, as demonstrated in Figure 6c,d, the discharge capacity is 100 mA h g^{-1} at a low current density of 20 mA g^{-1}. At current densities of 50 mA g^{-1}, 100 mA g^{-1}, 120 mA g^{-1}, and 150 mA g^{-1}, the discharge capacities are 73 mA h g^{-1}, 63 mA h g^{-1}, 61 mA h g^{-1}, and 60 mA h g^{-1}, respectively. When the current returns to 20 mA g^{-1}, the discharge capacity remains stable at ~100 mA h g^{-1}. It reveals that both STO and BTO materials are highly reversible. The change in discharge capacity during the first cycle arises from differences in the applied potential window. The broader potential range is

likely to enable additional electrochemical reactions or increased lithiation/delithiation processes, thereby influencing the overall discharge capacity.

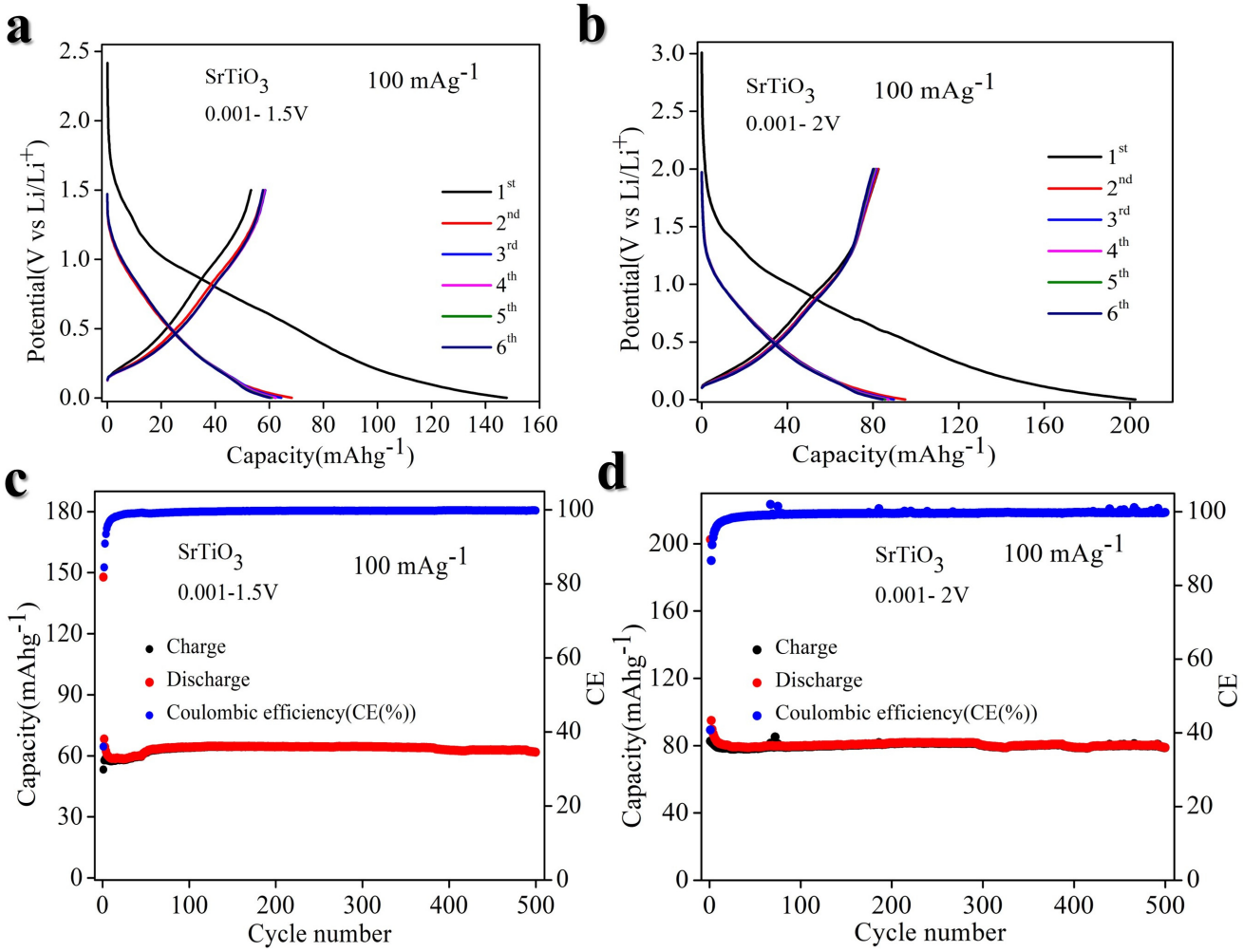


Figure 5. Electrochemical performance of STO at different voltage ranges in LIBs. (**a**) Galvanostatic charge–discharge (GCD) at 0.001–1.5 V. (**b**) Cyclic performance at 0.001–1.5 V. (**c**) Galvanostatic charge–discharge (GCD) at 0.001–2.0 V. (**d**) Cyclic performance at 0.001–2.0 V.

At wider voltage ranges, the stability of the solid electrolyte interphase (SEI) becomes critical. The SEI layer can become unstable under high voltage conditions, leading to increased side reactions that consume active lithium and degrade capacity. This instability is exacerbated by the presence of impurities or defects in the anode material that can promote unwanted reactions. In this context, BTO and STO were evaluated across three voltage ranges: 0.001–1.5 V, 0.001–2.0 V, and 0.001–2.5 V. The results indicated that the 0.001–1.5 V range exhibited superior stability in performance compared to the higher voltage settings. This suggests that limiting the operational voltage can enhance the integrity of the SEI, thereby improving overall battery efficiency and longevity [51].

The cyclic voltammetry profiles of BTO electrodes scanned at a rate of 0.1 mV s^{-1} reveal the presence of one broad reduction peak at 0.82 V vs. Li/Li^+ first cycles, accompanied by two corresponding broad oxidation peaks at 1.13 and 0.19 V vs. Li/Li^+ (Figure 7a). The galvanostatic lithiation–delithiation characterization of the BTO electrode exhibits an initial lithiation capacity of approximately 200 mA h g^{-1} and a delithiation capacity of 80 mA h g^{-1} during the first cycle, resulting in an initial Coulombic efficiency (CE) of 33% (Figure 4c). The observed low initial CE is attributable to the formation of the solid electrolyte interphase (SEI) below 1 V vs. Li/Li^+ (Figure 4c), structural disintegration, and

potential side reactions [52]. Enhancing the initial CE can be improved through the design of protective coatings or the modification of electrolyte composition by introducing suitable additives [53]. The CE increases to 85% in the second cycle and average CE ~99.9% in subsequent cycles (Figure 4a,b). A maximum delithiation capacity of ~100 mA h g^{-1} at 20 mA g^{-1} is achieved.

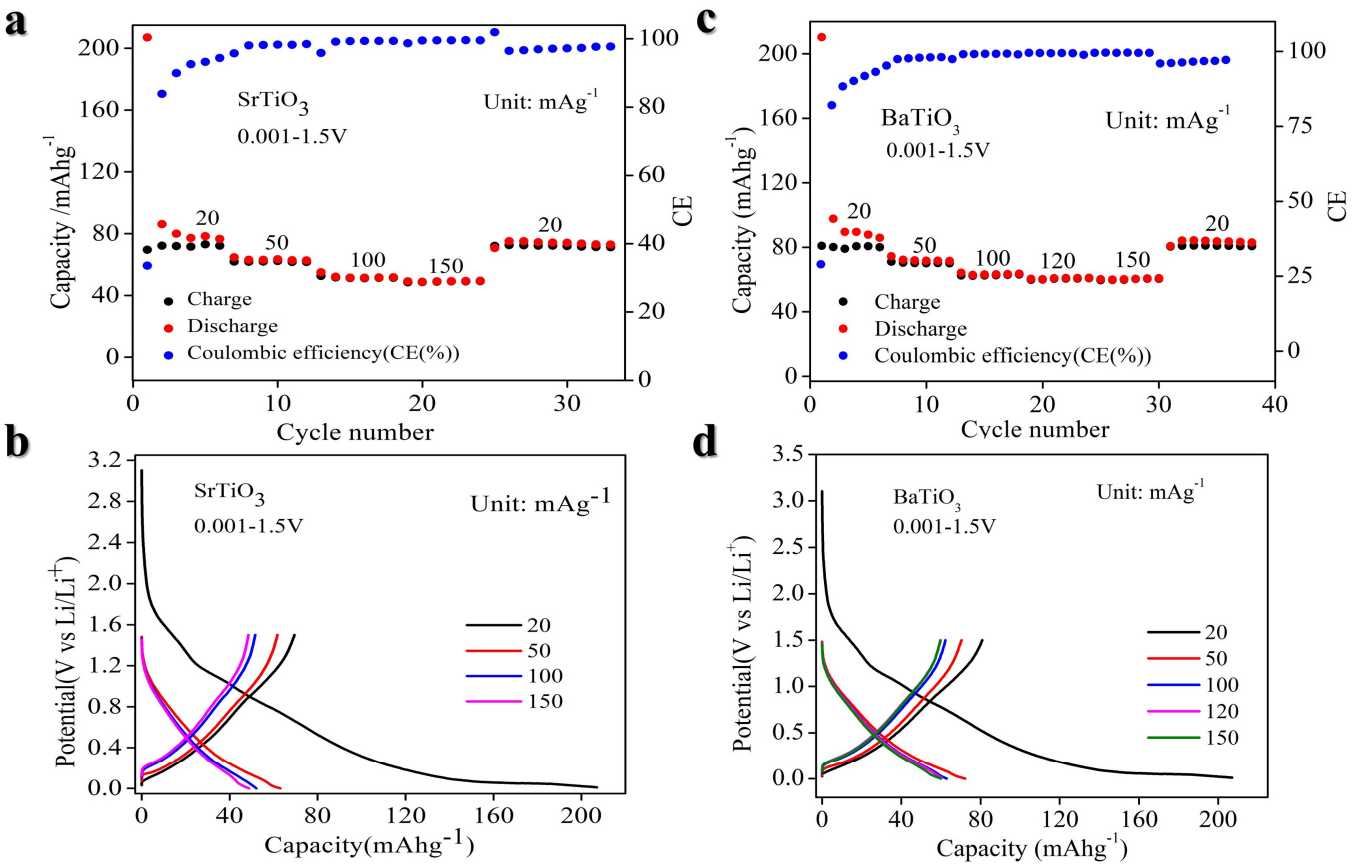


Figure 6. Rate performance of STO and BTO in 0.001–1.5 V. (**a**) STO rate performance in the range of 20 to 150 mA g^{-1}. (**b**) STO rate curve profile at different current densities in the range of 20 to 150 mA g^{-1}. (**c**) BTO rate performance in the range of 20 to 150 mA g^{-1}. (**d**) BTO discharge/charge voltage profile at different current densities in the range of 20 to 150 mA g^{-1}.

Similarly, for STO, the cyclic voltammetry (CV) analysis of STO electrodes at a scan rate of 0.1 mV s^{-1} demonstrates distinct electrochemical signatures. Specifically, the CV profile reveals a broad cathodic peak at approximately 0.82 V vs. Li/Li+ during the first cycle, accompanied by two corresponding broad anodic peaks at around 0.23 and 0.90 V vs. Li/Li^+ (Figure 7c). The galvanostatic lithiation–delithiation tests indicate an initial lithiation capacity of approximately 200 mA h g^{-1} and a delithiation capacity of 80 mA h g^{-1}, resulting in a low initial Coulombic efficiency (CE) of 40% (Figure 5b). This low initial CE is attributed to the formation of a solid electrolyte interphase (SEI) below 1 V vs. Li/Li^+, structural degradation, and potential side reactions. Strategies to enhance the initial CE include the application of protective coatings or modifications to the electrolyte composition by incorporating suitable additives. Notably, the CE improves to 94% in the second cycle and stabilizes at an average CE of approximately 99.9% in subsequent cycles (Figure 5a,b). The electrode achieves a maximum delithiation capacity of approximately 90 mA h g^{-1} at a current density of 20 mA g^{-1}. The galvanostatic lithiation–delithiation profiles of STO and BTO electrodes at various specific currents exhibit sloping profiles without distinct potential plateaus, indicating a solid-solution mechanism [27,54] (Figure 4a,b and Figure 5a,b). Additionally, at a current density of 20 mA g^{-1}, both STO and BTO electrodes demonstrate a low and stable average working potential of ~0.6 V vs.

Li/Li^+. Compared to previously reported anode materials such as spinel $Li_4Ti_5O_{12}$ [55] and perovskite $Li_{0.5}La_{0.5}TiO_3$ [27], the perovskite STO and BTO electrodes exhibit a lower average working potential (Figure 4a,b and Figure 5a,b), underscoring the potential of STO and BTO as promising anode materials for Li-ion batteries. The capacity can be increased by doping suitable elements.

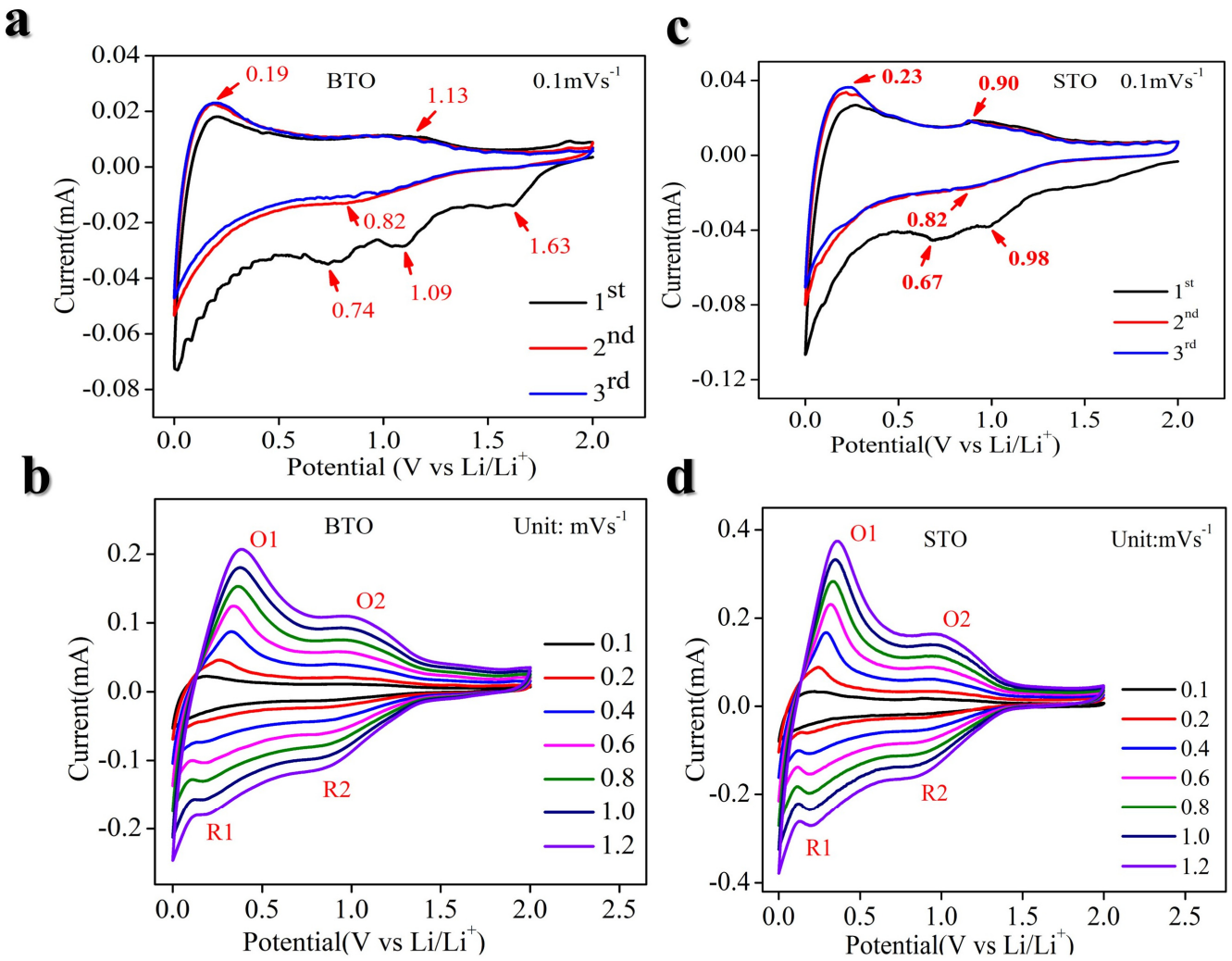


Figure 7. Cyclic voltammetry (CV) curves of the BTO and STO at room temperature. (**a**) CV of BTO in the first 3 cycles at a scan rate of 0.1 mV s^{-1}. (**b**) CV of BTO in the different scan rates of 0.1–1.2 mV s^{-1}. (**c**) CV of STO in the first 3 cycles at a scan rate of 0.1 mV s^{-1}. (**d**) CV of STO in the different scan rates of 0.1–1.2 mV s^{-1}.

Cyclic voltammetry (CV) works as an efficient technique to study the kinetics of electrode reactions as well. Theoretically, the voltametric response of an electroactive material at different scan rates can be described by the following power–law relationship [5,56], as in Equations (1) and (2):

$$i = av^b \quad (1)$$

$$\log i(v) = b \log v + \log a \quad (2)$$

Here, the response current (i) determined under a certain potential (V) follows a power–law dependence on the potential scan rate (v). Where the b-value, which is determined by the ion storage mechanism, can be calculated from the slope of the log (i)−log (v) plot. Specifically, a b-value of 0.5 indicates a completely diffusion-controlled process, while a b-value of 1.0 signifies either a faradaic contribution from charge transfer with surface or subsurface atoms (pseudocapacitance effect) or a non-faradaic contribution from

the electrical double-layer effect [54]. It has been well established that across a broad range of scan rates v, conventional materials $LiCoO_2$, $LiFePO_4$, and graphite demonstrate b ≈ 0.5. In contrast, pseudocapacitor materials, for example, Nb_2O_5, RuO_x, and MnO_2 materials, exhibit b ~ 1.0. This b-value should be a crucial reason for the much higher power capabilities of supercapacitors when compared to traditional rechargeable batteries (such as Li-ion, Ni-Cd, Pb-acid, and Ni-MH batteries) [54]. As shown in Figure 8a,b, the fact that the adjusted R^2 values anodic and cathodic of the linear fitting are approximately 1 is significant, as it indicates excellent chemical reversibility of the BTO and STO materials during charge and discharge processes, even at high scan rates [54]. As illustrated in Figure 8c, the redox reactions (i.e., charge/discharge processes) of the BTO- and STO-based electrodes exhibit b values of 0.88 and 0.90, indicating fast capacitive-controlled kinetics [27,54]. The data presented in Figure 8c further demonstrate that the electrode kinetics of the BTO- and STO-based electrodes are not controlled by diffusion processes only.

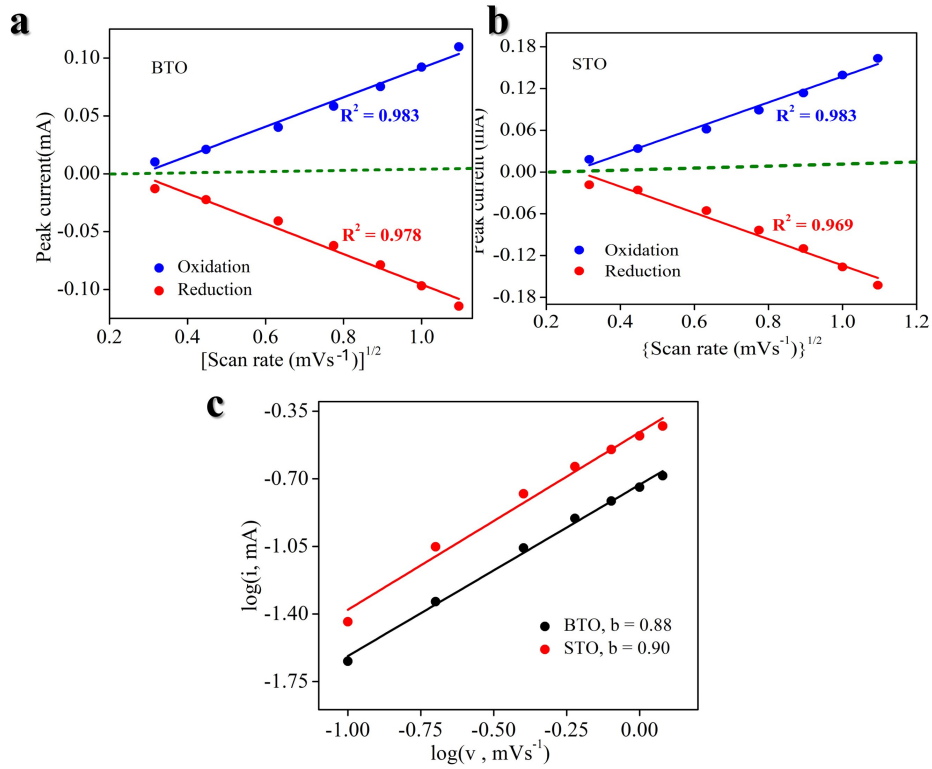


Figure 8. (**a**) Peak current (i) vs. $v^{1/2}$ (square root of scan rate (v)) of BTO. (**b**) Log (i) (peak current (i)) vs. log (v) (scan rate (v)) of STO. (**c**) Log (i) vs. log (v) of BTO and STO.

In order to understand the Li^+ storage mechanism STO (Figure 9a–c), X-Ray photoelectron spectroscopy (XPS) is utilized to explore the surface valence evolution to gain further insights into the origin capacity. The energy difference between O1s and Ti $2p_{3/2}$ levels ΔE increased to a higher value during the lithiation process (Figure 9a), evidencing the decrease in the Ti valence state [27]. At the same time, the Sr3d peak shows no obvious shift as expected for electrochemically inert Sr [29]. After full lithiation down to ≈0.001 V vs. Li/Li^+, no obvious Ti2p (Figure 9a) and Sr3d (Supporting Information Figure S6) peaks can be seen in the XPS spectrum. After delithiation to ≈2 V vs. Li/Li^+, the intensities of Ti 2p (Figure 9a) and Sr 3d (Supplementary Information Figure S6) peaks increase back. Also, after three cycles, Ti2p and Sr3d are also increased as before (Supplementary Information Figure S6).

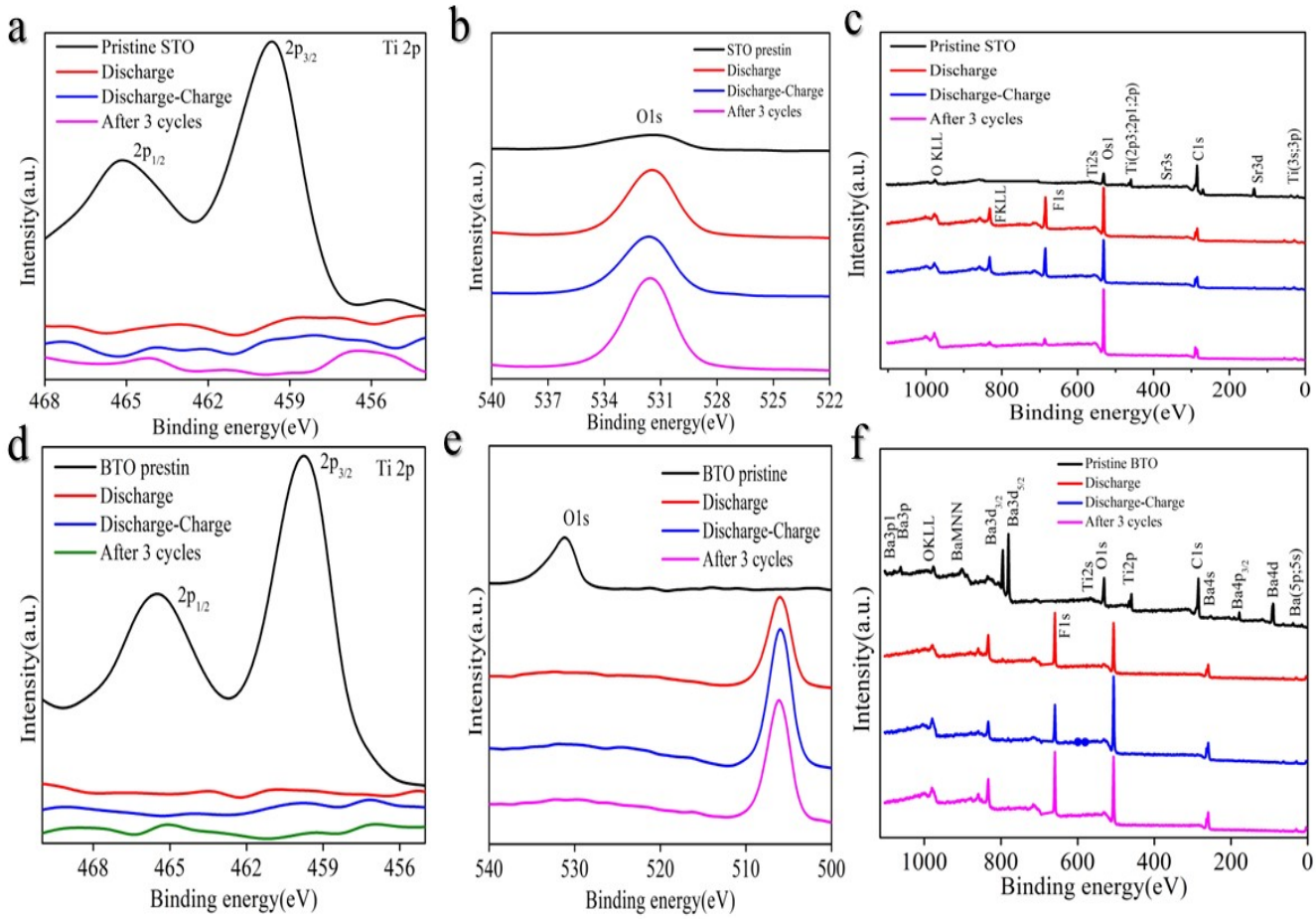


Figure 9. X-ray photoelectron spectroscopy (XPS) measurement. (**a**) Pristine STO, lithiation (discharge), lithiation–delithiation (discharge–charge), after 3 cycles. (**b**) O1s. (**c**) STO survey different conditions. (**d**) Pristine BTO, lithiation (discharge), lithiation–delithiation (discharge–charge), after 3 cycles. (**e**) O1s. (**f**) BTO survey different conditions.

In a similar manner, to elucidate the Li^+ storage mechanism in BTO (Figure 9d–f), XPS is employed to investigate the evolution of surface valence states, thereby gaining deeper insights into the origin of capacity. During the lithiation process, the energy difference (ΔE) between the O1s and Ti $2p_{3/2}$ levels increases, indicating a reduction in the Ti valence state as in Figure 9d. Simultaneously, the Ba3d peak remains largely unchanged (Supplementary Information Figure S6), consistent with the electrochemically inert nature of Ba as Sr. Upon full lithiation down to approximately 0.001 V vs. Li/Li^+, the XPS spectrum reveals the absence of evident Ti 2p (Figure 9d). Upon delithiation to around 2 V vs. Li/Li^+, the intensities of the Ti 2p peaks increase back.

We confirm that the XPS measurements were conducted ex situ. It can be pointed out that the surface of the cycled electrodes could have been influenced by the ex situ procedure, potentially leading to contamination or modifications during the transfer process. Ex situ methods can alter the electrode surface due to exposure to air or moisture after removal from the electrochemical cell, potentially leading to contamination or surface modifications. As a result, the changes detected by XPS may not fully represent the surface state during electrochemical cycling but rather reflect artifacts introduced during handling. Although XPS is a powerful tool for surface analysis, these limitations of ex situ techniques should be considered. In contrast, in situ or operando approaches offer more accurate analysis by preventing atmospheric exposure during measurement.

Figure 10a–d present the electrochemical impedance spectroscopy (EIS) [57] data for STO- (Figure 10a,b) and BTO (Figure 10c,d)-based electrodes under various conditions,

specifically prior to charging and following 40 cycles. The EIS spectra can be divided into three primary electrical components: internal resistance (R_Ω), electric double-layer capacitance (C_d), and faradaic impedance (Z_f). Faradaic impedance (Z_f) is further subdivided into charge transfer and mass transfer components, corresponding to high- and low-frequency regions, respectively [57,58]. The charge transfer component can be represented by charge transfer resistance (R_{ct}) and Warburg impedance (Z_w). The initial cell before charging displays low charge transfer resistance (R_{ct}). After 40 cycles, the R_{ct} progressively decreases, indicating the excellent stability and performance of the BTO- and STO-based electrodes.

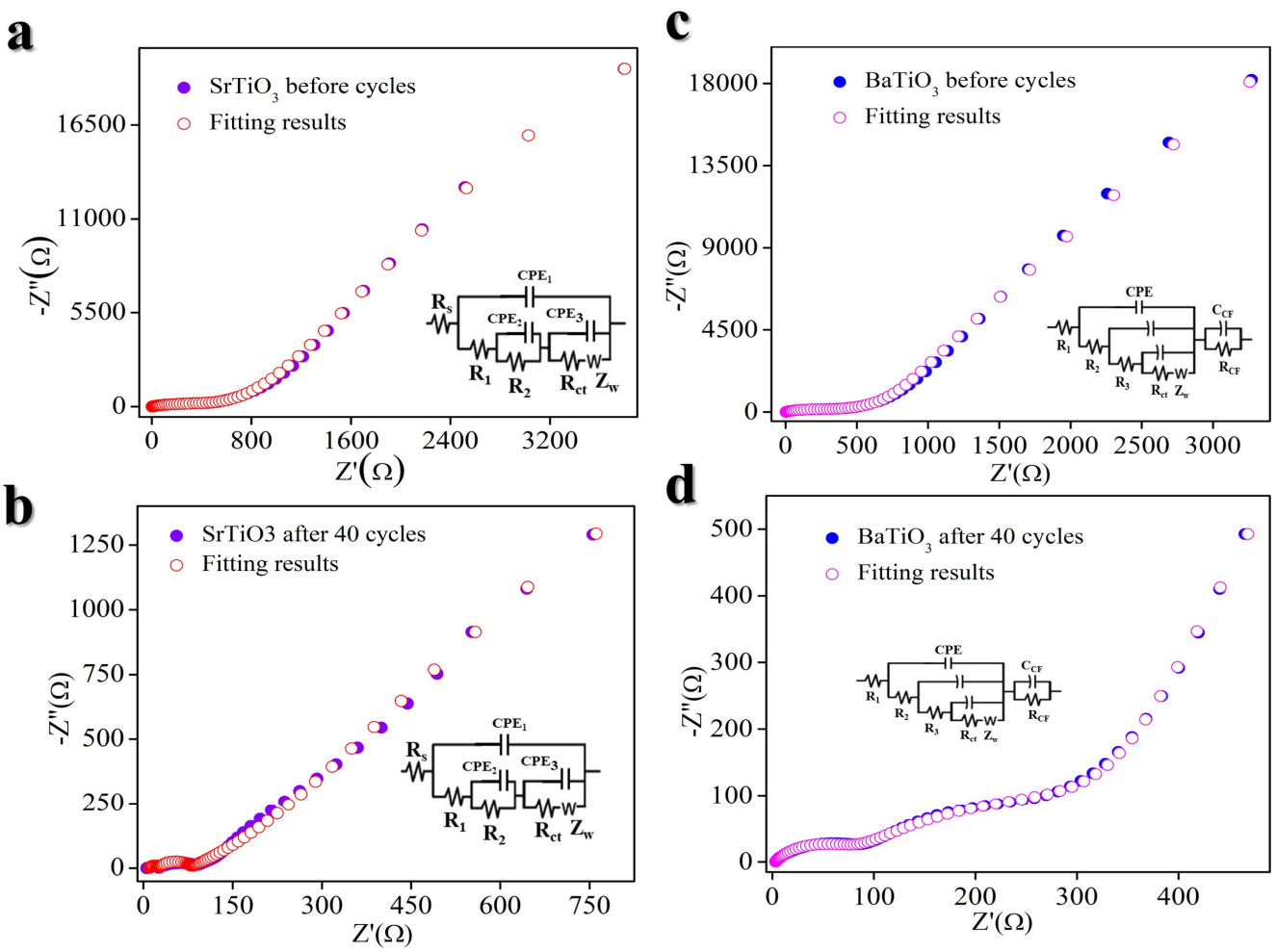


Figure 10. Electrochemical impedance spectroscopy (EIS) STO- and BTO-based electrodes. (**a**) STO before charging. (**b**) STO after 40 charge–discharge. (**c**) BTO before charging. (**d**) BTO after 40 cycles.

Faradaic impedance (Z_f) is further subdivided into charge transfer and mass transfer components, corresponding to high- and low-frequency regions, respectively. The charge transfer component can be represented by charge transfer resistance (R_{ct}) and Warburg impedance (Z_w). The initial cell before charging displays low charge transfer resistance (R_{ct}). After 40 cycles, the R_{ct} progressively decreases, indicating the excellent stability and performance of the BTO- and STO-based electrodes. It is that different circuit models can potentially provide equally good fits for the measured EIS (Electrochemical Impedance Spectroscopy) data. However, while various EECs may achieve a good fit for the Nyquist plot, it is essential that each element in the selected circuit has a clear physical meaning and accurately reflects the underlying electrochemical processes. Proper assignment and interpretation of these elements are crucial to ensure that the model represents the system's true behavior rather than merely offering a good mathematical fit.

4. Conclusions

In this investigation, we examined the Perovskite-based oxide compounds, namely $BaTiO_3$ and $SrTiO_3$ nanoparticles, as anode materials for lithium-ion batteries utilizing commercial nanopowders, $SrTiO_3$ and $BaTiO_3$ with standard carbonate-based electrolyte composed of 1M $LiPF_6$ (1:1 EC:DEC) with 10% FEC. The $SrTiO_3$ and $BaTiO_3$ electrodes exhibited a remarkable specific capacity of ~90 mA h g^{-1} at a low current density of 20 mA g^{-1}, a stable and low average operating potential of approximately 0.6 V vs. Li/Li^+, in addition to outstanding high-rate performance, maintaining a capacity of around 80 mA h g^{-1} over an extended cycling period of approximately 500 cycles at a high current density of 100 mA g^{-1}. Our findings demonstrate the feasibility of directly employing perovskite-type materials as anodes in lithium-ion batteries, underscoring their significant potential for lithium-ion storage. This research addresses the increasing market demands sustainably and paves the way for further exploration of various perovskite oxides as advanced anode materials for next-generation metal-ion batteries.

Supplementary Materials: The following supporting information can be downloaded at: https://www.mdpi.com/article/10.3390/nano14211723/s1, Figure S1: BTO energy dispersive X-Ray (EDX) spectrum. Figure S2: STO energy dispersive X-Ray (EDX) spectrum. Figure S3: (a) STO GCD profile at 0.001–2.5 V. (b) BTO GCD profile at 0.001–2.5 V. Figure S4: (a) STO cyclic performance at 0.001–2.5 V. (b) BTO cyclic performance at 0.001–2.5 V. Figure S5: Graphite, BTO, and STO GCD profile at 100 mA g^{-1}. Page S-6: The theoretical capacity of $BaTiO_3$ and $SrTi\ O_3$ electrode calculation. Figure S6: XPS of BTO (a) Before charging. (b) Discharge (lithiation). (c) Discharge–charge (lithiation–delithiation). (d) After 3 cycles. Figure S7: XPS of STO. Before charging, discharge (lithiation), discharge–charge (lithiation–delithiation), after 3 cycles.

Author Contributions: Conceptualization, N.O.; investigation, N.O.; data curation, N.O.; writing—original draft preparation, N.O.; review and editing, N.O., N.S. and R.S.K.; supervision, R.S.K.; funding acquisition, R.S.K., G.M. and B.R.W. All authors have read and agreed to the published version of the manuscript.

Funding: This work is financially supported by the NSF Center for the Advancement of Wearable Technologies (grant no. 1849243) and IRG2 NASA MIRO PR-SPRInT (grant no. 80NSSC19M0236).

Data Availability Statement: Data can be available upon request.

Acknowledgments: We thank the Molecular Science Research Center (MSRC), University of Puerto Rico, Puerto Rico, for providing the X-ray diffractometer (XRD), Scanning electron microscopy (SEM), and Energy Dispersive X-Ray (EDX). We sincerely thank William Perez for his assistance with the Raman characterization.

Conflicts of Interest: The authors declare no conflicts of interest.

References

1. Goodenough, J.B. Evolution of Strategies for Modern Rechargeable Batteries. *Acc. Chem. Res.* **2013**, *46*, 1053–1061. [CrossRef]
2. Goodenough, J.B.; Kim, Y. Challenges for Rechargeable Li Batteries. *Chem. Mater.* **2010**, *22*, 587–603. [CrossRef]
3. Armand, M.; Tarascon, J.M. Building Better Batteries. *Nature* **2008**, *451*, 652–657. [CrossRef] [PubMed]
4. Tarascon, J.M.; Armand, M. Issues and Challenges Facing Rechargeable Lithium Batteries. *Nature* **2001**, *414*, 359–367. [CrossRef] [PubMed]
5. Oli, N.; Flórez Gómez, J.F.; Zuluaga Gómez, C.C.; Katiyar, R.K.; Morell, G.; Katiyar, R.S. Revealing Underestimated Performance in the Bismuth Ferrite ($BiFeO_3$) Anode for High-Capacity and Long-Cycling Lithium-Ion Batteries. *ACS Appl. Energy Mater.* **2023**, *6*, 10853–10861. [CrossRef]
6. Xie, L.; Zhang, W.; Chen, X.; Shan, R.; Han, Q.; Qiu, X.; Oli, N.; Florez Gomez, J.F.; Zhu, L.; Wu, X.; et al. Bimetallic Cobalt-Nickel Selenide Nanocubes Embedded in a Nitrogen-Doped Carbon Matrix as an Excellent Li-Ion Battery Anode. *ACS Appl. Mater. Interfaces* **2023**, *15*, 25536–25549. [CrossRef]
7. Obrovac, M.N.; Chevrier, V.L. Alloy Negative Electrodes for Li-Ion Batteriesn. *Chem. Rev.* **2015**, *115*, 2043. Erratum in *Chem. Rev.* **2014**, *114*, 11444–11502. https://doi.org/10.1021/Cr500207g. [CrossRef]
8. Oli, N.; Choudhary, S.; Weiner, B.R.; Morell, G.; Katiyar, R.S. Comparative Investigation of Water-Based CMC and LA133 Binders for CuO Anodes in High-Performance Lithium-Ion Batteries. *Molecules* **2024**, *29*, 4114. [CrossRef]

9. Jin, Y.; Zhu, B.; Lu, Z.; Liu, N.; Zhu, J. Challenges and Recent Progress in the Development of Si Anodes for Lithium-Ion Battery. *Adv. Energy Mater.* **2017**, *7*, 1700715. [CrossRef]
10. Liu, C.; Han, M.; Cao, Y.; Chen, L.; Ren, W.; Zhou, G.; Chen, A.; Sun, J. Unlocking the Dissolution Mechanism of Phosphorus Anode for Lithium-Ion Batteries. *Energy Storage Mater.* **2021**, *37*, 417–423. [CrossRef]
11. Fugattini, S.; Gulzar, U.; Andreoli, A.; Carbone, L.; Boschetti, M.; Bernardoni, P.; Gjestila, M.; Mangherini, G.; Camattari, R.; Li, T.; et al. Binder-Free Nanostructured Germanium Anode for High Resilience Lithium-Ion Battery. *Electrochim. Acta* **2022**, *411*, 139832. [CrossRef]
12. Wachtler, M.; Besenhard, J.O.; Winter, M. Tin and Tin-Based Intermetallics as New Anode Materials for Lithium-Ion Cells. *J. Power Sources* **2001**, *94*, 189–193. [CrossRef]
13. Oli, N.; Castillo, D.C.L.; Weiner, B.R.; Morell, G.; Katiyar, R.S. Enhancing Electrochemical Performance of Si@CNT Anode by Integrating SrTiO3 Material for High-Capacity Lithium-Ion Batteries. *Molecules* **2024**, *29*, 4750. [CrossRef]
14. Costa, C.M.; Lizundia, E.; Lanceros-Méndez, S. Polymers for Advanced Lithium-Ion Batteries: State of the Art and Future Needs on Polymers for the Different Battery Components. *Prog. Energy Combust. Sci.* **2020**, *79*, 100846. [CrossRef]
15. Hochgatterer, N.S.; Schweiger, M.R.; Koller, S.; Raimann, P.R.; Wöhrle, T.; Wurm, C.; Winter, M. Silicon/Graphite Composite Electrodes for High-Capacity Anodes: Influence of Binder Chemistry on Cycling Stability. *Electrochem. Solid-State Lett.* **2008**, *11*, A76. [CrossRef]
16. Vorfolomeeva, A.A.; Stolyarova, S.G.; Asanov, I.P.; Shlyakhova, E.V.; Plyusnin, P.E.; Maksimovskiy, E.A.; Gerasimov, E.Y.; Chuvilin, A.L.; Okotrub, A.V.; Bulusheva, L.G. Single-Walled Carbon Nanotubes with Red Phosphorus in Lithium-Ion Batteries: Effect of Surface and Encapsulated Phosphorus. *Nanomaterials* **2023**, *13*, 153. [CrossRef]
17. Jin, H.; Wang, H.; Qi, Z.; Bin, D.-S.; Zhang, T.; Wan, Y.; Chen, J.; Chuang, C.; Lu, Y.-R.; Chan, T.-S.; et al. A Black Phosphorus–Graphite Composite Anode for Li-/Na-/K-Ion Batteries. *Angew. Chem.* **2020**, *132*, 2338–2342. [CrossRef]
18. Qin, J.; He, C.; Zhao, N.; Wang, Z.; Shi, C.; Liu, E.Z.; Li, J. Graphene Networks Anchored with Sn@Graphene as Lithium Ion Battery Anode. *ACS Nano* **2014**, *8*, 1728–1738. [CrossRef]
19. Schweidler, S.; De Biasi, L.; Schiele, A.; Hartmann, P.; Brezesinski, T.; Janek, J. Volume Changes of Graphite Anodes Revisited: A Combined Operando X-Ray Diffraction and in Situ Pressure Analysis Study. *J. Phys. Chem. C* **2018**, *122*, 8829–8835. [CrossRef]
20. Liu, Y.; Shi, H.; Wu, Z.S. Recent Status, Key Strategies and Challenging Perspectives of Fast-Charging Graphite Anodes for Lithium-Ion Batteries. *Energy Environ. Sci.* **2023**, *16*, 4834–4871. [CrossRef]
21. Zhang, S.S. Is Li/Graphite Half-Cell Suitable for Evaluating Lithiation Rate Capability of Graphite Electrode? *J. Electrochem. Soc.* **2020**, *167*, 100510. [CrossRef]
22. Hasegawa, G.; Kanamori, K.; Kiyomura, T.; Kurata, H.; Nakanishi, K.; Abe, T. Hierarchically Porous $Li_4Ti_5O_{12}$ Anode Materials for Li- and Na-Ion Batteries: Effects of Nanoarchitectural Design and Temperature Dependence of the Rate Capability. *Adv. Energy Mater.* **2015**, *5*, 1400730. [CrossRef]
23. Aghamohammadi, H.; Hassanzadeh, N.; Eslami-Farsani, R. A Review Study on Titanium Niobium Oxide-Based Composite Anodes for Li-Ion Batteries: Synthesis, Structure, and Performance. *Ceram. Int.* **2021**, *47*, 26598–26619. [CrossRef]
24. Sheng, Y.; Wang, Y.; Yin, S.; Zhao, L.; Zhang, X.; Liu, D.; Wen, G. Niobium-Based Oxide for Anode Materials for Lithium-Ion Batteries. *Chem. A Eur. J.* **2024**, *30*, e202302865. [CrossRef]
25. Ding, H.; Song, Z.; Zhang, H.; Li, X. Niobium-Based Oxide Anodes toward Fast and Safe Energy Storage: A Review. *Mater. Today Nano* **2020**, *11*, 100082. [CrossRef]
26. Yang, L.; Xiong, X.; Liang, G.; Li, X.; Wang, C.; You, W.; Zhao, X.; Liu, X.; Che, R. Atomic Short-Range Order in a Cation-Deficient Perovskite Anode for Fast-Charging and Long-Life Lithium-Ion Batteries. *Adv. Mater.* **2022**, *34*, 2200914. [CrossRef]
27. Zhang, L.; Zhang, X.; Tian, G.; Zhang, Q.; Knapp, M.; Ehrenberg, H.; Chen, G.; Shen, Z.; Yang, G.; Gu, L.; et al. Lithium Lanthanum Titanate Perovskite as an Anode for Lithium Ion Batteries. *Nat. Commun.* **2020**, *11*, 3490. [CrossRef]
28. Nguyen, A.T.; Nguyen, T.N.; Mittova, V.O.; Thieu, Q.Q.V.; Mittova, I.Y.; Tran, V.M.; Nguyen, M.T.; Nguyen, D.Q.; Kim, I.T.; Nguyen, T.L. Tailored Synthesis of NdMnxFe1-XO3 Perovskite Nanoparticles with Oxygen-Vacancy Defects for Lithium-Ion Battery Anodes. *Heliyon* **2023**, *9*, e21782. [CrossRef]
29. Li, X.; Lin, Z.; Jin, N.; Yang, X.; Du, Y.; Lei, L.; Rozier, P.; Simon, P.; Liu, Y. Perovskite-Type $SrVO_3$ as High-Performance Anode Materials for Lithium-Ion Batteries. *Adv. Mater.* **2022**, *34*, 2107262. [CrossRef]
30. Chang, L.; Li, J.; Le, Z.; Nie, P.; Guo, Y.; Wang, H.; Xu, T.; Xue, X. Perovskite-Type $CaMnO_3$ Anode Material for Highly Efficient and Stable Lithium Ion Storage. *J. Colloid Interface Sci.* **2021**, *584*, 698–705. [CrossRef]
31. Yue, B.; Hu, Q.; Yu, W.; Ma, Q.; Bao, Y.; Li, L.; Wang, J.; Liu, G.; Dong, X.; Liu, J. Perovskite-Type $RMnO_3$ (R = La, Nd, Eu) Nanofibers with Fast Li+ Transport Properties as Anode for Lithium-Ion Batteries. *Mater. Today Commun.* **2023**, *36*, 106459. [CrossRef]
32. Hüger, E.; Riedel, L.; Zhu, J.; Stahn, J.; Heitjans, P.; Schmidt, H.; Hüger, E.; Riedel, L.; Zhu, J.; Stahn, J.; et al. Lithium Niobate for Fast Cycling in Li-Ion Batteries: Review and New Experimental Results. *Batteries* **2023**, *9*, 244. [CrossRef]
33. Chintha, S.; Atif, S.; Chaupatnaik, A.; Golubnichiy, A.; Abakumov, A.M.; Barpanda, P. $Na_{0.5}Bi_{0.5}TiO_3$ Perovskite Anode for Lithium-Ion Battery. *Sustain. Energy Fuels* **2024**, *8*, 5058–5064. [CrossRef]
34. Huang, J.; Hu, L.; Yang, Z.; Li, J.; Wang, P.; Wei, Y.; Sun, P. Hollow Spherical $LaFeO_3$ Perovskite as Anode Material for Lithium-Ion Battery. *Inorg. Chem. Commun.* **2023**, *150*, 110458. [CrossRef]

35. Yue, B.; Hu, Q.; Ji, L.; Wang, Y.; Liu, J. Facile Synthesis of Perovskite $CeMnO_3$ Nanofibers as an Anode Material for High Performance Lithium-Ion Batteries. *RSC Adv.* **2019**, *9*, 38271–38279. [CrossRef] [PubMed]
36. Zhang, C.; Zhang, Y.; Nie, Z.; Wu, C.; Gao, T.; Yang, N.; Yu, Y.; Cui, Y.; Gao, Y.; Liu, W. Double Perovskite La_2MnNiO_6 as a High-Performance Anode for Lithium-Ion Batteries. *Adv. Sci.* **2023**, *10*, 2300506. [CrossRef]
37. Roy, K.; Li, T.; Ogale, S.; Robertson, N. Hybrid Perovskite-like Iodobismuthates as Low-Cost and Stable Anode Materials for Lithium-Ion Battery Applications. *J. Mater. Chem. A Mater.* **2021**, *9*, 2689–2693. [CrossRef]
38. Kostopoulou, A.; Vernardou, D.; Makri, D.; Brintakis, K.; Savva, K.; Stratakis, E. Highly Stable Metal Halide Perovskite Microcube Anodes for Lithium-Air Batteries. *J. Power Sources Adv.* **2020**, *3*, 100015. [CrossRef]
39. Atif, S.; Chaupatnaik, A.; Rao, A.; Padhy, A.; Chintha, S.; Nukala, P.; Fichtner, M.; Barpanda, P. Perovskite Oxides with Pb at B-Site as Li-Ion Battery Anodes. *Electrochim. Acta* **2024**, *502*, 144838. [CrossRef]
40. Tewari, N.; Shivarudraiah, S.B.; Halpert, J.E. Photorechargeable Lead-Free Perovskite Lithium-Ion Batteries Using Hexagonal $Cs_3Bi_2I_9$Nanosheets. *Nano Lett.* **2021**, *21*, 5578–5585. [CrossRef]
41. Wang, J.; Wang, M.; Xiao, J.; Dong, J.; Li, Y.; Zhang, L.; Si, J.; Pan, B.C.; Chen, C.S.; Chen, C. hua A Microstructure Engineered Perovskite Super Anode with Li-Storage Life of Exceeding 10,000 Cycles. *Nano Energy* **2022**, *94*, 106972. [CrossRef]
42. Johnson, D.C.; Prieto, A.L. Use of Strontium Titanate (SrTiO3) as an Anode Material for Lithium-Ion Batteries. *J. Power Sources* **2011**, *196*, 7736–7741. [CrossRef]
43. Da Silva, L.F.; Avansi, W.; Moreira, M.L.; Mesquita, A.; Maia, L.J.Q.; Andrés, J.; Longo, E.; Mastelaro, V.R. Relationship between Crystal Shape, Photoluminescence, and Local Structure in $SrTiO_3$ Synthesized by Microwave-Assisted Hydrothermal Method. *J. Nanomater.* **2012**, *2012*, 890397. [CrossRef]
44. Gong, W.; Yun, H.; Ning, Y.B.; Greedan, J.E.; Datars, W.R.; Stager, C.V. Oxygen-Deficient $SrTiO_{3-x}$, x = 0.28, 0.17, and 0.08. Crystal Growth, Crystal Structure, Magnetic, and Transport Properties. *J. Solid. State Chem.* **1991**, *90*, 320–330. [CrossRef]
45. Akilarasan, M.; Tamilalagan, E.; Chen, S.M.; Maheshwaran, S.; Chen, T.W.; Al-Mohaimeed, A.M.; Al-Onazi, W.A.; Elshikh, M.S. An Eco-Friendly Low-Temperature Synthetic Approach towards Micro-Pebble-Structured GO@$SrTiO_3$ Nanocomposites for the Detection of 2,4,6-Trichlorophenol in Environmental Samples. *Microchim. Acta* **2021**, *188*, 72. [CrossRef]
46. Ehrambaf, L.; Setoudeh, N.; Ali, M.; Zamani, A.; Hayati, R. Characterization of Synthesized $SrTiO_3$ from Purified Celestite Concentrate Using Mechanochemical Process. *Inorg. Chem. Res.* **2022**, *6*, 130–138. [CrossRef]
47. Biglar, M.; Gromada, M.; Stachowicz, F.; Trzepieciński, T. Synthesis of Barium Titanate Piezoelectric Ceramics for Multilayer Actuators (MLAs). *Acta Mech. Autom.* **2017**, *11*, 275–279. [CrossRef]
48. Korkmaz, S.; Kariper, I.A. $BaTiO_3$-Based Nanogenerators: Fundamentals and Current Status. *J. Electroceramics* **2021**, *48*, 8–34. [CrossRef]
49. Badapanda, T.; Senthil, V.; Panigrahi, S.; Anwar, S. Diffuse Phase Transition Behavior of Dysprosium Doped Barium Titanate Ceramic. *J. Electroceramics* **2013**, *31*, 55–60. [CrossRef]
50. Jamil, M.S.; Saputro, K.E.; Noviyanto, A.; Widayatno, W.B.; Wismogroho, A.S.; Amal, M.I.; Rochman, N.T.; Nishimura, T. Dense and Fine-Grained Barium Titanate Prepared by Spark Plasma Sintering. *J. Phys. Conf. Ser.* **2019**, *1191*, 012039. [CrossRef]
51. Peled, E.; Menkin, S. Review—SEI: Past, Present and Future. *J. Electrochem. Soc.* **2017**, *164*, A1703–A1719. [CrossRef]
52. Krumov, M.R.; Lang, S.; Johnson, L.; Abruña, H.D. Operando Investigation of Solid Electrolyte Interphase Formation, Dynamic Evolution, and Degradation During Lithium Plating/Stripping. *ACS Appl. Mater. Interfaces* **2023**, *15*, 47692–47703. [CrossRef] [PubMed]
53. Hou, Z.; Zhang, J.; Wang, W.; Chen, Q.; Li, B.; Li, C. Towards High-Performance Lithium Metal Anodes via the Modification of Solid Electrolyte Interphases. *J. Energy Chem.* **2020**, *45*, 7–17. [CrossRef]
54. Dong, X.; Chen, L.; Liu, J.; Haller, S.; Wang, Y.; Xia, Y. Environmentally-Friendly Aqueous Li (or Na)-Ion Battery with Fast Electrode Kinetics and Super-Long Life. *Sci. Adv.* **2016**, *2*, e1501038. [CrossRef]
55. Yuan, T.; Tan, Z.; Ma, C.; Yang, J.; Ma, Z.F.; Zheng, S. Challenges of Spinel $Li_4Ti_5O_{12}$ for Lithium-Ion Battery Industrial Applications. *Adv. Energy Mater.* **2017**, *7*, 1601625. [CrossRef]
56. Liu, J.; Wang, J.; Xu, C.; Jiang, H.; Li, C.; Zhang, L.; Lin, J.; Shen, Z.X. Advanced Energy Storage Devices: Basic Principles, Analytical Methods, and Rational Materials Design. *Adv. Sci.* **2018**, *5*, 1700322. [CrossRef]
57. Westerhoff, U.; Kroker, T.; Kurbach, K.; Kurrat, M. Electrochemical Impedance Spectroscopy Based Estimation of the State of Charge of Lithium-Ion Batteries. *J. Energy Storage* **2016**, *8*, 244–256. [CrossRef]
58. Westerhoff, U.; Kurbach, K.; Lienesch, F.; Kurrat, M. Analysis of Lithium-Ion Battery Models Based on Electrochemical Impedance Spectroscopy. *Energy Technol.* **2016**, *4*, 1620–1630. [CrossRef]

Disclaimer/Publisher's Note: The statements, opinions and data contained in all publications are solely those of the individual author(s) and contributor(s) and not of MDPI and/or the editor(s). MDPI and/or the editor(s) disclaim responsibility for any injury to people or property resulting from any ideas, methods, instructions or products referred to in the content.